

1 **Organic matter in carbonaceous chondrite lithologies of Almahata Sitta: Incorporation of**
2 **previously unsampled carbonaceous chondrite lithologies into ureilitic regolith**

3

4 Yoko Kebukawa^{1*}, Michael. E. Zolensky², Cyrena A. Goodrich³, Motoo Ito⁴, Nanako O. Ogawa⁵,
5 Yoshinori Takano⁵, Naohiko Ohkouchi⁵, Kento Kiryu¹, Motoko Igisu⁶, Takazo Shibuya⁶, Matthew A.
6 Marcus⁷, Takuji Ohigashi⁸, James Martinez⁹, Yu Kodama¹⁰, Muawia H. Shaddad¹¹, and Peter
7 Jenniskens¹²

8

9 *Corresponding author email: kebukawa@ynu.ac.jp

10

11 ¹ Department of Chemistry and Life Science, Yokohama National University, 79-5 Tokiwadai,
12 Hodogaya-ku, Yokohama 240-8501, Japan

13 ² Astromaterials Research and Exploration Science, NASA Johnson Space Center, 2101 NASA
14 Parkway, Houston, TX 77058, USA

15 ³ Lunar and Planetary Institute, Universities Space Research Association-Houston, 3600 Bay Area
16 Blvd, Houston, TX 77058 USA,

17 ⁴ Kochi Institute for Core Sample Research, Japan Agency for Marine-Earth Science and Technology
18 (JAMSTEC), B200 Monobe, Nankoku, Kochi 783-8502, Japan

19 ⁵ Biogeochemistry Research Center (BGC), Japan Agency for Marine-Earth Science and Technology
20 (JAMSTEC), 2-15 Natsushima-Cho, Yokosuka 237-0061, Japan

21 ⁶ Super-cutting-edge Grand and Advanced Research (Sugar) Program, Institute for Extra-cutting-
22 edge Science and Technology Avant-garde Research (X-star), Japan Agency for Marine-Earth
23 Science and Technology (JAMSTEC), 2-15 Natsushima-cho, Yokosuka 237-0061, Japan

24 ⁷ Advanced Light Source, Lawrence Berkeley National Laboratory, 1 Cyclotron Road, Berkeley, CA
25 94720, USA

26 ⁸ UVSOR Synchrotron, Institute for Molecular Science, 38 Nishigo-Naka, Myodaiji, Okazaki 444-

27 8585, Japan

28 ⁹ Jacobs Engineering, NASA Johnson Space Center, 2101 NASA Parkway, Houston, TX 77058, USA

29 ¹⁰ Marine Works Japan Ltd., B200 Monobe, Nankoku, Kochi 783-8502, Japan

30 ¹¹ Physics Department, University of Khartoum, Khartoum 11115, Sudan

31 ¹² SETI Institute, 189 Bernardo Ave, Mountain View, CA 94043, USA

32

33 **Abstract**

34 The Almahata Sitta (AhS) meteorite is a unique polymict ureilite. Recently, carbonaceous chondritic
35 lithologies were identified in AhS. Organic matter (OM) is ubiquitously found in primitive
36 carbonaceous chondrites. The molecular and isotopic characteristics of this OM reflect its origin and
37 parent body processes, and are particularly sensitive to heating. The C1-lithologies, AhS 671 and
38 AhS 91A were investigated, focusing mainly on the OM. We found that the OM in these lithologies
39 is unique and contains primitive isotopic signatures, but experienced slight heating possibly by short-
40 term heating event(s). These characteristics support the idea that one or more carbonaceous
41 chondritic bodies were incorporated into the ureilitic parent body. The uniqueness of the OM in the
42 AhS samples implies that there were large variations in primitive carbonaceous chondritic materials
43 in the Solar System other than known primitive carbonaceous chondrite groups such as CI, CM, and
44 CR chondrites.

45

46 **INTRODUCTION**

47 Organic matter (OM) is ubiquitously found in primitive carbonaceous chondrites (CCs). The
48 majority of OM is found in the form of complex macromolecular organic materials that are often
49 referred to as insoluble organic matter (IOM). The fraction of soluble organic matter (SOM) is
50 relatively small, but its compositional variation is huge—thousands of different molecular formulae
51 exist including further alteration products of organic molecules (e.g., Orthous-Daunay et al. 2019;
52 Schmitt-Kopplin et al. 2010). The total amount of OM in thermally metamorphosed carbonaceous,

53 ordinary, and enstatite chondrites is drastically lower compared to unheated (CI, CM, and CR) CCs,
54 due to high temperature processing which decomposes the OM (e.g., Alexander et al. 2007). The
55 elemental and isotopic compositions and molecular structures of OM reflect their parent body
56 processes and are particularly sensitive to heating (e.g., Alexander et al. 2007; Alexander et al. 2010;
57 Kebukawa et al. 2011; Quirico et al. 2018). Thus, OM in chondrites can be used as indicators of
58 thermal events (Busemann et al. 2007; Cody et al. 2008; Kebukawa et al. 2010). In contrast, with the
59 exception of ureilites, differentiated meteorites rarely contain carbonaceous compounds other than
60 xenolithic material.

61
62 The ureilites are a group of primitive achondrites. Main group ureilites mainly consist of olivine and
63 pyroxene, and are characterized by high abundances of carbon, principally in the form of well-
64 crystalline graphite as well as minor diamond. They represent the residual mantle of a carbon-rich
65 parent asteroid that experienced high-temperature igneous processing and partial differentiation early
66 in the history of the solar system (Collinet and Grove 2020; Goodrich et al. 2015; Goodrich et al.
67 2007; Mittlefehldt et al. 1998; Scott et al. 1993; Warren and Kallemeyn 1992). Polymict ureilites are
68 breccias consisting of mixed ureilitic materials, as well as an important component of xenolith clasts,
69 including multiple chondritic and non-ureilitic achondrite types. Polymict ureilites represent regolith
70 formed on ureilitic offspring bodies that accreted as rubble piles after catastrophic disruption of a
71 primordial ureilite parent body (e.g., Goodrich et al. 2015). The Almahata Sitta (AhS) meteorite is
72 considered to be an anomalous polymict ureilite. AhS originated from the impact of the near-earth
73 asteroid 2008 TC₃, which is tentatively classified as an F-type asteroid (a subtype in C complex) in
74 spectroscopic taxonomy (Jenniskens et al. 2009). The asteroid disintegrated in the atmosphere and
75 the recovered stones, which include a wide variety of different meteorite types, represent clasts from
76 the pre-impact breccia. Approximately 50-70% of the AhS stones are ureilitic materials and the rest
77 include a wide variety of chondritic materials—including enstatite, ordinary, Rumuruti-type, and
78 carbonaceous chondrites (Goodrich et al. 2015 and references therein). The chondritic materials are

79 equivalent to the xenolithic clasts in typical polymict ureilites.

80

81 Carbonaceous chondritic lithologies AhS 671 and AhS 91/91A were first found among the AhS
82 stones and characterized by Goodrich et al. (2019). These lithologies are xenoliths—not genetically
83 related to ureilites—consisting mainly of C1 material, enclosing minor fragments of ureilitic olivine
84 and pyroxene, as well as ordinary chondrite and enstatite chondrite fragments (Goodrich et al. 2019).
85 The C1 lithologies contain phyllosilicates (serpentine and saponite), amorphous material, magnetite,
86 breunnerite, dolomite, fayalitic olivine, an unidentified Ca-rich silicate phase, Fe, Ni sulfides, and
87 minor Ca-phosphate, and ilmenite (Goodrich et al. 2019). The bulk oxygen isotope compositions of
88 the C1 lithology are $\delta^{18}\text{O} = 13.53\text{‰}$ and $\delta^{17}\text{O} = 8.93\text{‰}$ which are unlike those of any known
89 chondrites, but similar to the compositions of several CC-like clasts in typical polymict ureilites
90 (Goodrich et al. 2019).

91

92 To elucidate the nature of the OM and the origin of carbonaceous chondritic lithologies, we
93 conducted structural, elemental and isotopic analyses of OM in AhS 671 and AhS 91A with micro-
94 Fourier transform infrared spectroscopy (μFTIR), Raman microspectroscopy, scanning transmission
95 X-ray microscopy (STXM), and elemental analyzer/isotope ratio mass spectrometry (EA/IRMS). We
96 further characterized AhS 671 with nanoscale secondary isotope mass spectrometry (NanoSIMS) and
97 secondary electron microscopy (SEM).

98

99 **METHODS**

100 **Bulk Carbon and Nitrogen Contents and Their Isotopic Compositions**

101 For the measurements of total carbon and nitrogen contents and their isotopic compositions, we used
102 an automated EA/IRMS system (Flash EA1112 elemental analyzer/ConFlo III interface/Delta Plus
103 XP isotope-ratio mass spectrometer, Thermo Finnigan Co., Bremen) at JAMSTEC, which was
104 modified to improve the sensitivity for small sample analysis ($>100\text{ ngN}$, $>500\text{ ngC}$) (Isaji et al.

2020; Ogawa et al. 2010). This analysis was conducted at the same time by the same methods as our previous measurement of the carbonaceous clast in the Zag meteorite (Kebukawa et al. 2020). Subsamples of AhS 671 and AhS 91A were rinsed with an organic solvent mixture (dioxin-analysis-grade dichloromethane and methanol, FUJIFILM Wako Pure Chemical Corporation, Japan, 1:1 by volume) to remove contaminants from the surface, and then dried under a gentle flow of argon gas at ambient temperature. Sample aliquots weighing 12 to 629 μg were weighed in a pre-cleaned tin capsule (3.5×4 mm smooth wall capsules, Ludi Co., Swiss) and folded into a small packet before being introduced into the EA/IRMS. The forceps and tin capsules used in this study were pre-cleaned in the mixed solvent described above. The carbon and nitrogen contents and their isotopic compositions were calibrated using three reference materials covering from -34.17‰ to $+0.49\text{‰}$ for $\delta^{13}\text{C}$ and from $+0.86\text{‰}$ to $+61.53\text{‰}$ for $\delta^{15}\text{N}$, including: L-tyrosine (BG-T; C: 59.7%, N: 7.74%, $\delta^{13}\text{C}$: $-20.83 \pm 0.10\text{‰}$, $\delta^{15}\text{N}$: $+8.74 \pm 0.09\text{‰}$) (Tayasu et al. 2011), nickel octaethylporphyrin (Ni-OEP; C: 73.0%, N: 9.47%, $\delta^{13}\text{C}$: $-34.17 \pm 0.06\text{‰}$, $\delta^{15}\text{N}$: $+0.86 \pm 0.03\text{‰}$) (Ogawa et al. 2010), L-valine (USGS75; C: 51.3 %, N: 12.0%, $\delta^{13}\text{C}$: $+0.49 \pm 0.07\text{‰}$, $\delta^{15}\text{N}$: $+61.53 \pm 0.14\text{‰}$) (Schimmelmann et al. 2016). The analytical errors for the isotopic compositions estimated by repeated analyses of BG-T and Ni-OEP are $\pm 0.39\text{‰}$ (s.d. 1σ , $n=11$, $0.58\text{--}12.8 \mu\text{gC}$) for $\delta^{13}\text{C}$ and $\pm 0.66\text{‰}$ (s.d. 1σ , $n=12$, $0.08\text{--}1.7 \mu\text{gN}$) for $\delta^{15}\text{N}$.

122

123 **Micro Fourier Transform Infrared Spectroscopy**

124 For micro-FTIR analysis, a small amount of material from the clasts was pressed between two KBr
125 plates ($\sim 5 \times 5 \times 1 \text{ mm}^3$). IR absorption spectra were collected using a micro-FTIR (JASCO FT/IR-
126 6100+IRT-5200), equipped with a ceramic IR light source, a germanium-coated KBr beam splitter, a
127 mercury-cadmium-telluride (MCT) detector, and $\times 16$ Cassegrain mirrors, at Yokohama National
128 University. A total of 256 scans of IR transmission spectra were accumulated with a wavenumber
129 resolution of 4 cm^{-1} , in the wavenumber range of $7000\text{--}400 \text{ cm}^{-1}$, with a $50 \times 50 \mu\text{m}^2$ aperture.
130 Background spectra were acquired through blank areas of the KBr adjacent to the samples.

131

132 **Raman Microspectroscopy**

133 A few hundred micrometer-sized grains from AhS 671 and AhS 91A were pressed into gold
134 substrates (0.1 mm-thick) with glass slides, and analyzed using a Raman microspectrometer
135 (Nanophoton RAMANtouch) with a 532 nm laser at JAMSTEC. The spot size was $<1 \mu\text{m}$ using
136 $\times 100$ objective with the numerical aperture of 0.90, and the laser power at the sample surface was
137 $<700 \mu\text{W}$. The spectral range was $100\text{--}2600 \text{ cm}^{-1}$ with a 600 grooves/mm grating. The exposure time
138 for each spectrum was 20 s and two accumulations were obtained for each analytical spot to discard
139 cosmic ray events in the detector. The Raman shift was calibrated using a silicon wafer prior to
140 analyses.

141

142 The peak positions (ω_D and ω_G), the full width at half-maximum (FWHM, Γ_D and Γ_G), and the
143 peak intensity ratio (I_D/I_G) of defect (D: $\sim 1350 \text{ cm}^{-1}$) band and graphite (G: $\sim 1590 \text{ cm}^{-1}$) band were
144 determined by peak fitting to the Lorentzian and BWF (Breit–Wigner–Fano), respectively—so called
145 L–BWF model (Ferrari and Robertson 2000)—with a linear baseline correction between $900\text{--}1800$
146 cm^{-1} , following the method in Kiryu et al. (2020).

147

148 **FIB**

149 Ultrathin sections (approximately 100 nm thick) were prepared from AhS 671 and AhS 91A using a
150 focused ion beam (FIB) apparatus (SMI-4050), at Kochi Institute for Core Sample Research,
151 JAMSTEC. The sections ($14 \times 12 \times 0.1 \mu\text{m}^3$ for AhS 671 and $12 \times 10 \times 0.1 \mu\text{m}^3$ for AhS 91A) were
152 extracted using the FIB with a Ga^+ ion beam at 30 kV then finished with a lower accelerating voltage
153 of 5 kV. These sections were mounted on a commercial FIB grid with W deposition.

154

155 **STXM/XANES**

156 Carbon X-ray absorption near-edge structure (C-XANES) analyses were performed using the STXM

157 at beamline 5.3.2.2 of the Advanced Light Source (ALS), Lawrence Berkeley National Laboratory
158 (Kilcoyne et al. 2003). Microspectral images stacks at the C *K*-edge were acquired with energy step
159 sizes (ΔE) of 0.1 eV in 283-295.5 eV region, 0.5 eV in 280-283 eV and 295.5-301.0 eV regions, and
160 1 eV in 301-310 eV region, with a dwell time of 5 ms and 0.1-0.2 μm steps per pixel. C-XANES peak
161 intensity maps were obtained from these image data sets. An image representing the amount of
162 aromatic/olefinic C was obtained by subtracting the optical density (OD, $-\ln(\text{transmission}/I_0)$) image
163 at 283 eV (pre-edge) from that at 285.2 eV. Similarly, a carbonate image was defined as the difference
164 between the OD at 290.2 eV and that at 289.5 eV. Energy calibration was performed using the C 1s \rightarrow
165 $3s\sigma_g$ transition of CO₂ gas at 292.74 eV (Prince et al. 1999).

166

167 Fe-XANES analyses were performed using the STXM at BL4U of the UVSOR, Institute for Molecular
168 Science. The Fe *L*₃-edge-XANES spectra were acquired with ΔE of 0.2 eV in 705-724 eV region, and
169 1 eV in 700-705 eV and 724-730 eV regions, with a dwell time of 3 ms and 0.2 μm steps per pixel.
170 The Fe-XANES spectral component map was obtained using the singular value decomposition (SVD)
171 method (e.g., Koprinarov et al. 2002) from a “stack” image data set, in order to visualize the
172 distribution of three different spectral components. Energy calibration was performed using the F 1s
173 $\rightarrow a_{1g}$ transition of SF₆ gas at 688 eV.

174

175 The elemental maps were obtained by acquiring pairs of images below (I_1) and on the absorption edges
176 (I_2), at 280 and 292 eV, respectively for C *K*-edge, 525 eV and 539 eV for O *K*-edge, and 705 eV and
177 709 eV for Fe *L*₃-edge, with a dwell time of 3-5 ms, and taking the $-\ln(I_2/I_1)$ for each pixel, with 0.05-
178 0.1 μm steps per pixel. STXM/XANES data analysis was performed using the software aXis2000
179 (<http://unicorn.mcmaster.ca/aXis2000.html>).

180

181 **NanoSIMS**

182 After the STXM, we analyzed the FIB-prepared-sections of AhS 671 and AhS 91A by ion imaging

183 with the JAMSTEC NanoSIMS 50L at Kochi Institute for Core Sample Research, JAMSTEC. A
184 typical measurement involved rastering a focused primary Cs⁺ beam (~100 nm diameter, ~1 pA)
185 across 18 × 18 μm² areas for AhS 671 and 24 × 24 μm² areas for AhS 91A (256 × 256 pixels) for 20
186 cycles with an acquisition time of 5 ms/pixel (328 sec/frame). The ¹²C, ¹³C, ¹⁶O, ¹²C¹⁴N, ¹²C¹⁵N, and
187 ³²S were measured as negative secondary ions simultaneously in six electron multipliers. Secondary
188 electrons were detected along with the secondary ions.

189

190 After C and N isotope analysis of the sample, we conducted a measurement of H isotopes (¹H and
191 ²H) and ¹²C as negative secondary ions together with secondary electrons. A focused Cs⁺ primary
192 beam (~200 nm diameter, ~3 pA) was rastered over 18 × 18 μm² areas for AhS 671 and 24 × 24 μm²
193 areas for AhS 91A, and 256 × 256 pixel images were acquired for 20 cycles with an acquisition time
194 of 10 ms/pixel (655 sec/frame).

195

196 Measurement was started after stabilization of the secondary ion intensities following a pre-
197 sputtering procedure of approximately 10 min. The sample was coated with a 10 nm Au thin film to
198 mitigate electrostatic charging on the surface. The final images were generated from regions that had
199 statistically enough counts. The carbon-rich regions were chosen by distributions of ¹²C within a
200 section applying 10% threshold of total ¹²C ion counts. The H, C and N isotopic compositions were
201 calculated following analytical routines using a standard organic material (1-hydroxybenzotriazole
202 hydrate; C₆H₅N₃O·xH₂O) (Ito et al. 2014). The isotopic images were processed using the custom
203 written software “NASA JSC imaging software for NanoSIMS” developed in the Interactive Data
204 Language (IDL) program (Ito and Messenger 2008).

205

206 **Secondary Electron Microscopy**

207 Back-scattered electron images (BEI), elemental X-ray maps, and transmission Kikuchi diffraction
208 (TKD) measurements were obtained from the FIB slice of AhS 671 using a Supra 55 variable

209 pressure FEG-SEM with a Bruker Electron Back-Scattered Diffraction (EBSD) system in the
 210 Materials Evaluation Laboratory, Structural Engineering Division, Johnson Space Center (JSC). X-
 211 ray mapping on the Supra 55 FEG-SEM utilized a Bruker energy dispersive spectrometer (EDS). We
 212 previously determined that a column pressure of 9 Pa and no C-coating on the sample was optimal
 213 for TKD. We used 320×240 pattern pixelation, frame averaging of 3, 20 kV, a working distance of
 214 14.9 mm, pixel size of 1.95 μm , and low extractor voltage to yield an acceptable balance of hit rate,
 215 mapping speed and map quality using an exposure time of 30 ms (gain 650). The TKD maps took 1
 216 to 9 h to acquire.

217

218 RESULTS

219 Bulk Elemental and Isotopic Analyses

220 The bulk C and N abundances and the $\delta^{13}\text{C}$ and $\delta^{15}\text{N}$ values of AhS 671 and AhS 91A are
 221 summarized in [Table 1](#) and [Fig. 1](#). These values were considerably different between AhS 671 and
 222 91A. The C abundances in AhS 91A were smaller than in AhS 671. The N abundances in AhS 91A
 223 were much smaller than in AhS 671, and thus N/C ratios of AhS 91A were smaller than in AhS 671.
 224 The C and N abundances and isotope ratios were variable among each AhS 91A sample aliquots,
 225 indicating high heterogeneity in this sample compared with AhS 671 (at least among our AhS 91A
 226 and AhS 671 sample aliquots).

227

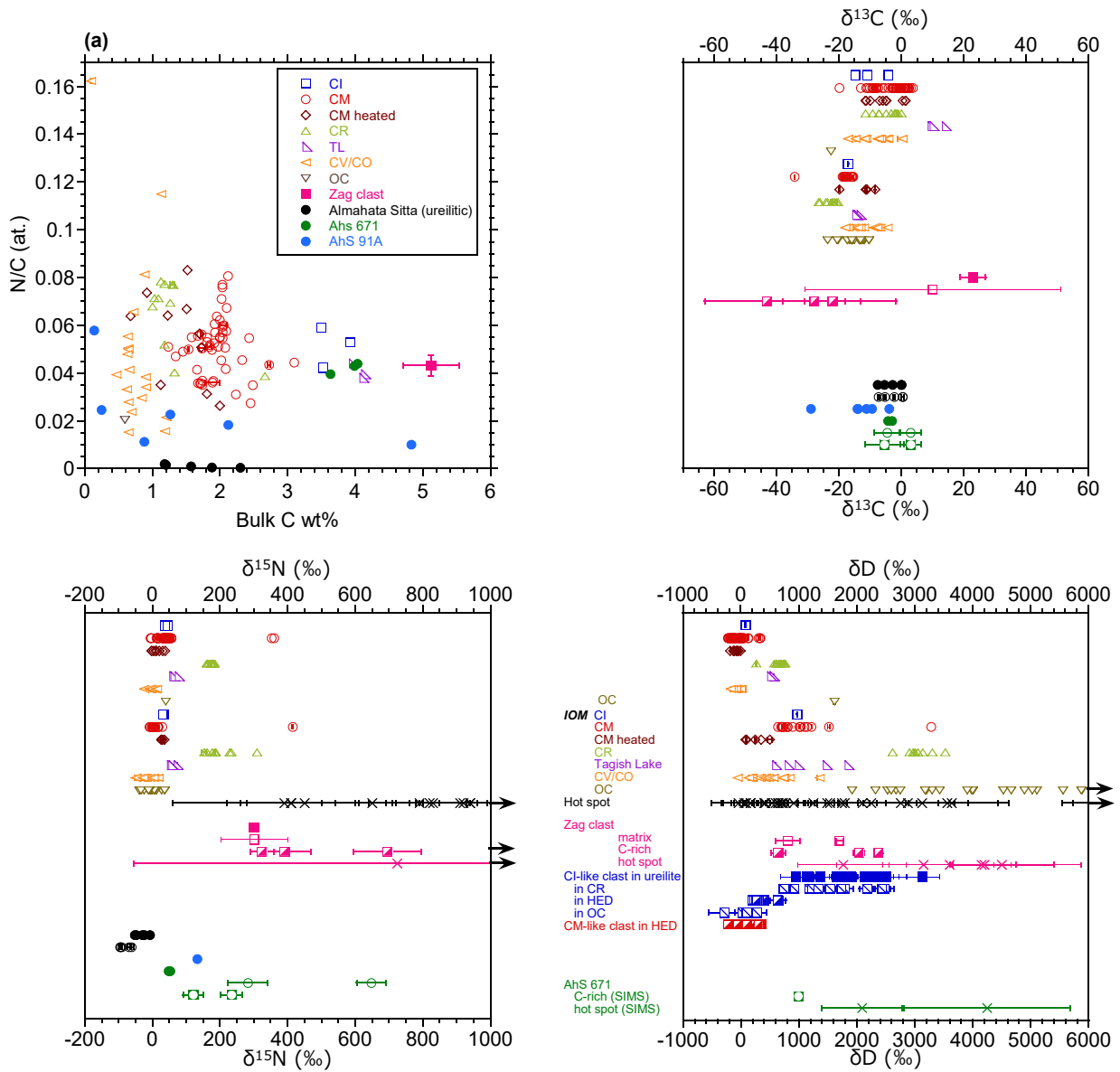
228 Table 1. Bulk C and N elemental and isotope analysis of AhS 671 and AhS 91A.

		Sample					
		weight (mg)	C wt%	$\delta^{13}\text{C}$ ‰	N wt%	$\delta^{15}\text{N}$ ‰	N/C at.
AhS 671	Run#1	0.052	3.6	-4.3	0.17	+52.5	0.040
	Run#2	0.093	4.0	-4.3	0.20	+47.6	0.043
	Run#3	0.043	4.0	-3.0	0.21	+51.4	0.044
	Average		3.9 ±0.2	-3.8 ±0.7	0.19 ±0.02	+50.5 ±2.6	0.042 ±0.002
AhS 91A	Run#1	0.012	4.8	-29.0	0.056	n.d.	0.010

Run#2	0.033	2.1	-13.9	0.045	n.d.	0.018
Run#3	0.092	0.88	-14.1	0.012	n.d.	0.011
Run#4	0.214	n.d.	n.d.	n.d.	n.d.	n.d.
Run#5	0.177	1.3	-11.2	0.033	+133	0.023
Run#6	0.629	0.25	-3.9	0.007	n.d.	0.025
Run#7	0.435	0.14	-9.5	0.009	n.d.	0.058
Average		1.6 ±1.7	-13.6 ±9.1	0.027 ±0.021		0.024 ±0.018

229 Errors are standard deviation (1σ). n.d.= not determined.

230



232 Fig. 1: Elemental and isotopic composition of AhS samples 91A and 671 compared with previously

233 obtained values for various chondrites, AhS ureilitic lithologies, CI- and CM-like clasts in ureilites,
234 and a xenolithic clast in the Zag ordinary chondrite. (a) Bulk C abundance (wt.%) vs. N/C ratio
235 (atomic), (b) $\delta^{13}\text{C}$, (c) $\delta^{15}\text{N}$, and (d) δD . Data from Alexander et al. (2007, 2010) for IOM from
236 chondrites; Herd et al. (2011) for Tagish Lake IOM; Alexander et al. (2012) for bulk chondrites;
237 Busemann et al. (2006) and Hashiguchi et al. (2015) for hot spots; Downes et al. (2015) for AhS
238 ureilitic lithologies; Kebukawa et al. (2019b, 2020) for the Zag clast; Patzek et al. 2020 GCA for CI-
239 and CM-like clasts.

240

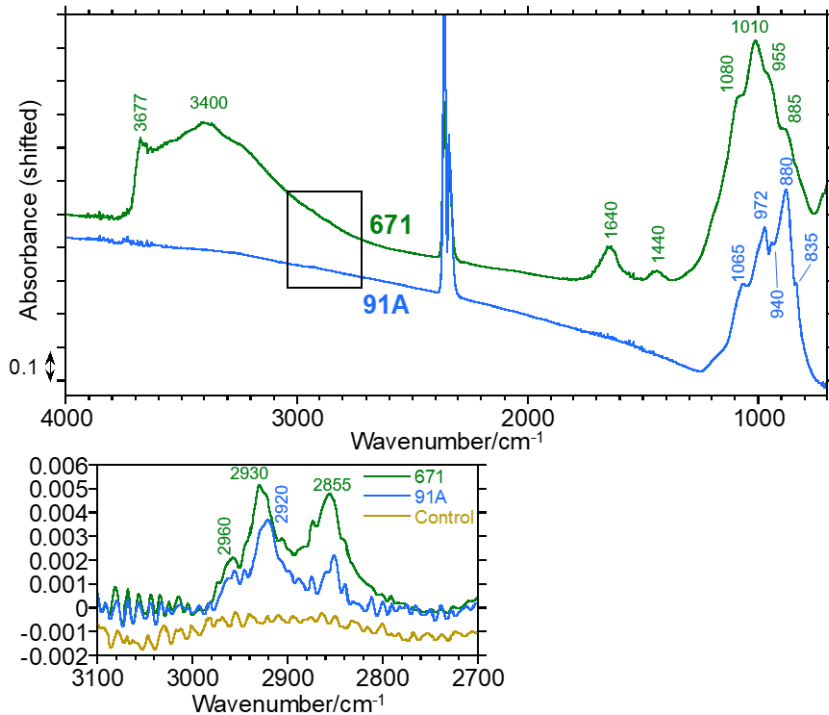
241 **Micro-FTIR Spectra**

242 [Fig. 2](#) shows IR absorption spectra of AhS 671 and AhS 91A. Little to no organic features were
243 visible in both AhS 671 and AhS 91A at around 2900 cm^{-1} where aliphatic C–H peaks appear.
244 Enlarged and baseline corrected spectra in the region of aliphatic C–H ([Fig. 2, lower panel](#)) showed
245 small peaks at 2960 , $2920\text{--}30$, and 2855 cm^{-1} due to aliphatic CH_3 asymmetric stretching, aliphatic
246 CH_2 asymmetric stretching, and aliphatic CH_3+CH_2 symmetric stretching, respectively. Considering
247 that control spectra (baked antigorite) showed no peaks at this region, these peaks in AhS 671 and
248 AhS 91A are likely indigenous. The CH_2/CH_3 peak height ratios were ~ 2.4 for both AhS 671 and
249 AhS 91A, which was much higher than the values of typical CCs ($\sim 1\text{--}1.5$; (Kebukawa et al. 2019a).

250

251 The IR spectrum of AhS 671 showed a broad band around 3400 cm^{-1} with a shoulder at 3677 cm^{-1}
252 which was characteristic of phyllosilicate OH with some adsorbed/interlayer water. A peak at 1010
253 cm^{-1} was consistent with Si–O in phyllosilicates. Small shoulders at 1080 , 955 , and 885 cm^{-1} were
254 likely due to Ca-rich pyroxene. A peak at 1440 cm^{-1} was assigned to carbonates. A peak at 1640 cm^{-1}
255 can be assigned to adsorbed/interlayer water. The IR spectrum of AhS 91A only showed silicate
256 features with the peaks at 972 and 880 cm^{-1} , and small shoulders at 1065 , 940 , and 835 cm^{-1} . These
257 silicate features were likely due to olivine with some contribution of pyroxene, considering that
258 olivine is known to have main Si–O peaks at $\sim 990\text{--}960\text{ cm}^{-1}$ and $\sim 890\text{--}870\text{ cm}^{-1}$ with a small peak at

259 $\sim 950\text{-}930\text{ cm}^{-1}$, in which higher Mg numbers tend to have these peaks at higher wavenumber
 260 (Salisbury et al. 1991). Also, diopside has Si-O peaks at $\sim 1080\text{ cm}^{-1}$, 970 cm^{-1} , and 870 cm^{-1} with a
 261 small peak at $\sim 920\text{ cm}^{-1}$, and enstatite shows Si-O peaks at $\sim 1080\text{-}1060\text{ cm}^{-1}$ and $\sim 1010\text{ cm}^{-1}$ with a
 262 small peaks at $\sim 960\text{-}930\text{ cm}^{-1}$ (Salisbury et al. 1991).
 263



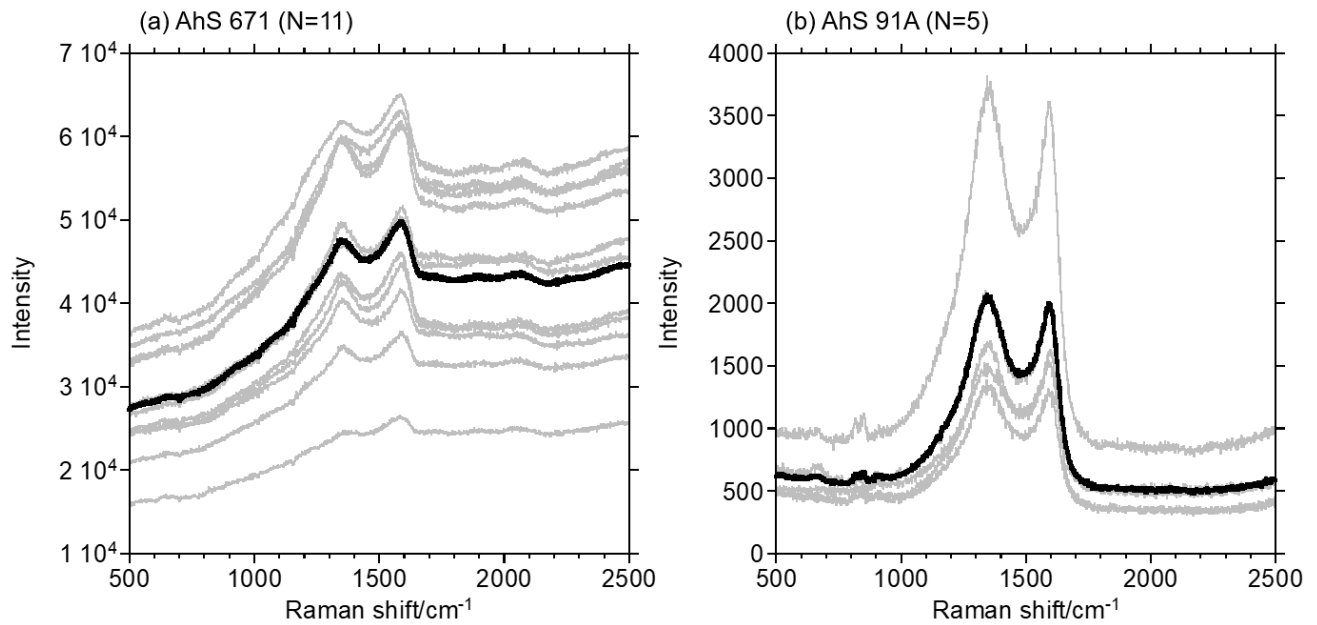
265 Fig. 2: Infrared absorption spectra of AhS 671 and AhS 91A. Enlarged aliphatic C-H regions (a linear
 266 baseline between $3100\text{-}2700\text{ cm}^{-1}$ was subtracted) are shown in the lower panel with control
 267 (antigorite baked at $500\text{ }^{\circ}\text{C}$).
 268

269 Raman Spectra

270 Fig. 3 shows the Raman spectra of AhS 671 and AhS 91A. The D band and the G band were shown
 271 in the first order region of the Raman spectra. The peak position (ω), the FWHM (Γ), and the peak
 272 intensity ratio (I_D/I_G) of the D band and G band obtained by peak fitting are shown in Fig. 4 and
 273 Table 2. The Raman parameters of these two AhS fragments do not follow the metamorphic trends of
 274 CCs. Although AhS 91A was somewhat in between the type 2 CC group (Murchison (CM2), Tagish
 275 Lake (C2-ung), Y-793321 (CM2-heated); Kiryu et al. 2020) and the thermally metamorphosed CC

276 group (Allende (CV3.2), Moss (CO3.6); Kiryu et al. 2020), AhS 671 was completely off from the
277 trends and large heterogeneity was observed. The absolute intensity of D and G bands of AhS 91A
278 were significantly lower than those of AhS 671 (Fig. 3). Although the absolute intensities are
279 affected not only by concentration of sample but also by the surface conditions and so on, this is
280 consistent with the results of the bulk elemental analysis that AhS 91A was poor in OM (Table 1 and
281 Fig. 1).

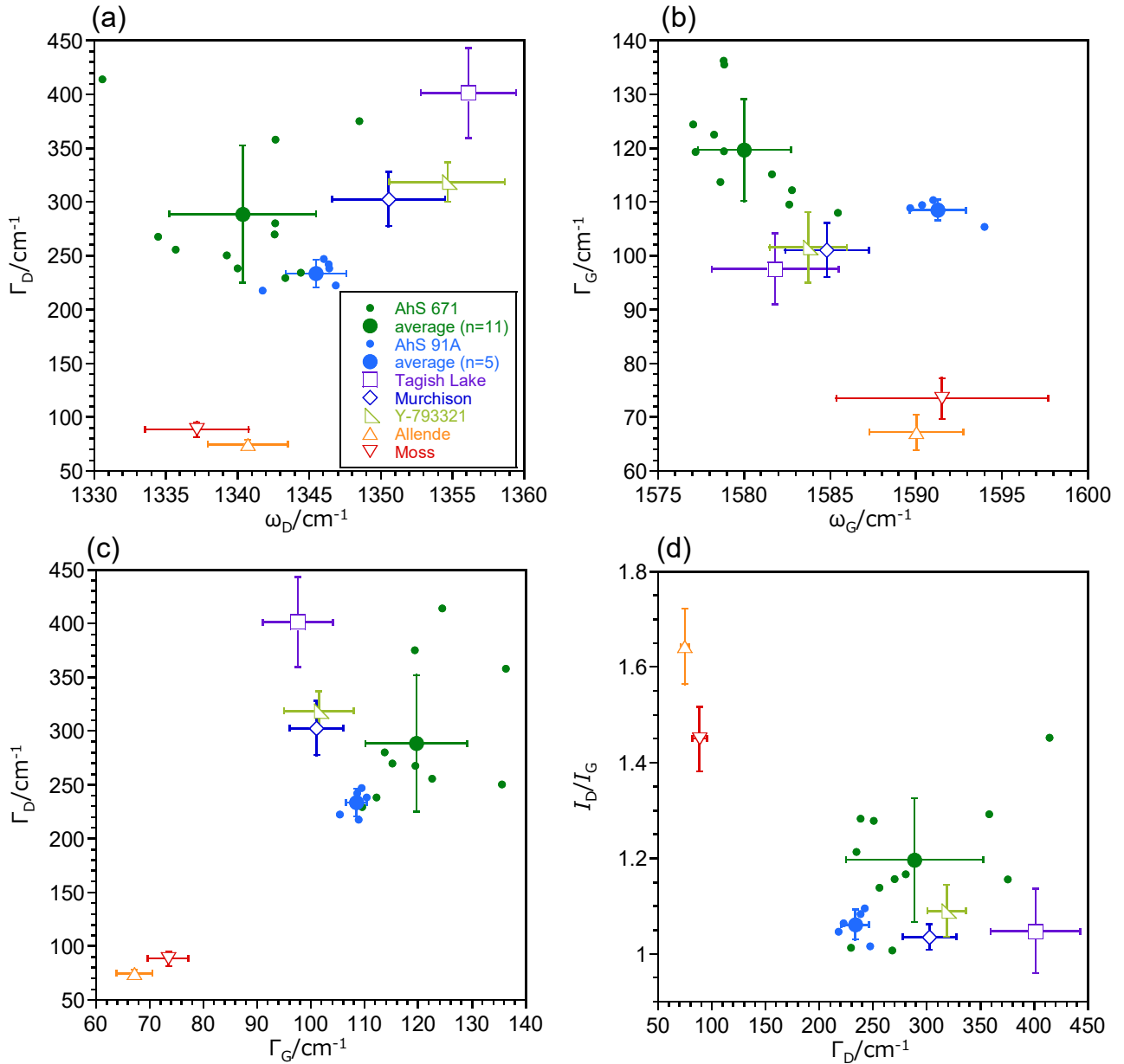
282



285 Fig. 3: Raman spectra of (a) AhS 671 and (b) AhS 91A. The spectra from each spot are shown in
286 gray, and average spectra are shown in black.

287

288



290 Fig. 4: The Raman D and G band parameters of AhS 671 and AhS 91A compared with various
 291 carbonaceous chondrites. (a) the D band peak position vs. the full width half-maximum (FWHM) of
 292 D band, (b) the G band peak position vs. FWHM of G band, (c) FWHM of G band vs. FWHM of D
 293 band, and (d) FWHM of D band vs. the peak intensity ratio of D and G bands (I_D/I_G). The data of
 294 Murchison (CM2), Tagish Lake (C2-ung), Allende (CV3.2), Moss (CO3.6), and Yamato (Y-)793321
 295 (CM2-heated) is from Kiryu et al. (2020).

296

297 Table 2: Raman D and G band parameters of AhS 671 and AhS 91A. Chondrite data are from Kiryu

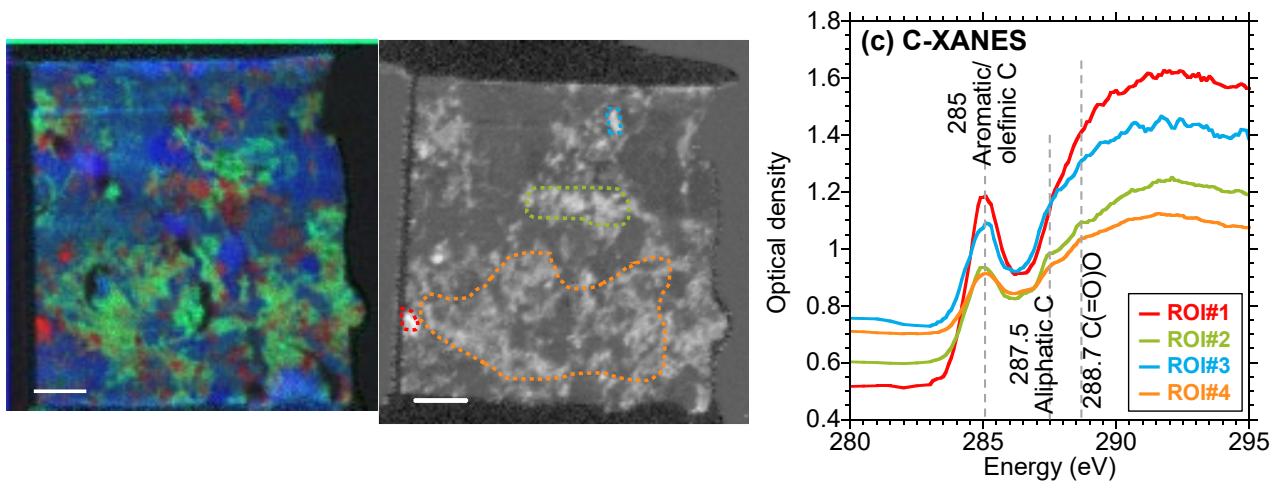
		ω_D/cm^{-1}	Γ_D/cm^{-1}	ω_G/cm^{-1}	Γ_G/cm^{-1}	I_D/I_G
AhS 671	Point#1	1343	358	1579	136.3	1.29
	Point#2	1334	268	1579	119.5	1.01
	Point#3	1339	251	1579	135.5	1.28
	Point#4	1344	234	1585	108.0	1.21
	Point#5	1343	270	1582	115.2	1.16
	Point#6	1331	414	1577	124.5	1.45
	Point#8	1336	256	1578	122.6	1.14
	Point#9	1348	375	1577	119.3	1.16
	Point#10	1340	238	1583	112.2	1.28
	Point#11	1343	280	1579	113.8	1.17
	Point#12	1343	230	1583	109.6	1.01
	Average (n=11)	1340 \pm 5	289 \pm 64	1580 \pm 3	119.7 \pm 9.5	1.20 \pm 0.13
AhS 91A	Point#1	1342	218	1590	108.9	1.05
	Point#2	1346	242	1591	108.6	1.10
	Point#3	1346	247	1590	109.4	1.02
	Point#4	1347	222	1594	105.4	1.06
	Point#5	1346	238	1591	110.4	1.08
	Average (n=5)	1345 \pm 2	234 \pm 13	1591 \pm 2	108.5 \pm 1.9	1.06 \pm 0.03
Tagish Lake	C2-ung	1356 \pm 3	401 \pm 42	1582 \pm 4	97.6 \pm 6.6	1.05 \pm 0.09
Murchison	CM2	1351 \pm 4	303 \pm 25	1585 \pm 2	101.1 \pm 5.0	1.04 \pm 0.03
Y-793321	CM2 heated	1355 \pm 4	319 \pm 18	1584 \pm 2	101.6 \pm 6.5	1.09 \pm 0.05
Allende	CV3	1341 \pm 3	75 \pm 4	1590 \pm 3	67.2 \pm 3.3	1.64 \pm 0.08
Moss	CO3.6	1337 \pm 4	89 \pm 7	1592 \pm 6	73.5 \pm 3.8	1.45 \pm 0.07

299

300 **STXM/XANES**

301 STXM images of the FIB section taken from AhS 671 are shown in [Fig. 5a and b](#). C-XANES spectra
302 from regions of interest (ROIs) in the FIB section are shown in [Fig. 5c](#). The STXM elemental maps
303 showed that sub-micrometer C-rich grains/aggregates were scattered over the FIB section
304 particularly in Fe-rich regions ([Fig. 5a](#)). C-XANES spectra of the C-rich areas showed peaks at 285.0
305 eV assigned to aromatic/olefinic C with small features at 287.5 eV assigned to aliphatic C and at

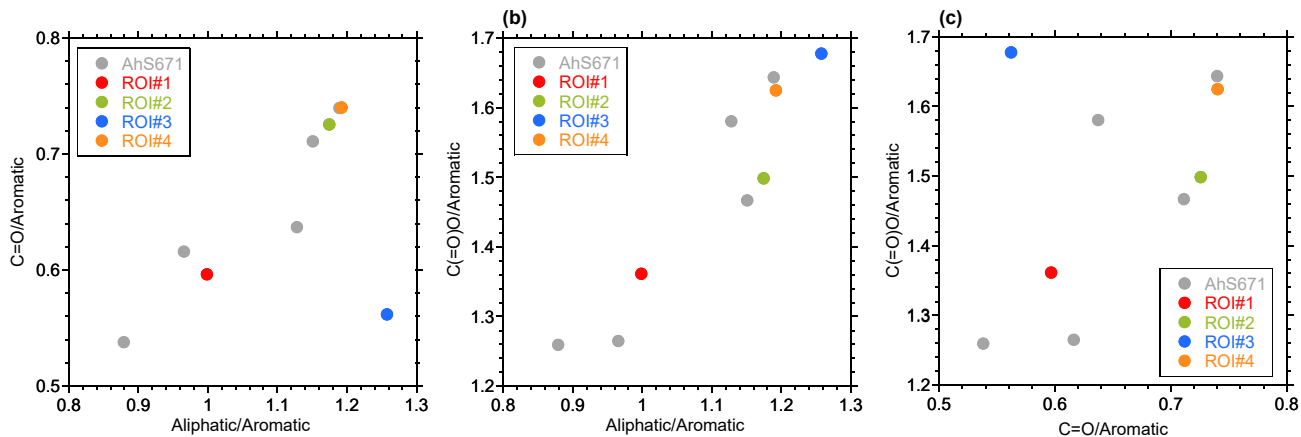
306 288.7 eV assigned to carboxyl/ester C(=O)O (Fig. 5c). ROI#1 in Fig. 5b was condensed OM. The
307 “condensed” nature was characterized by the C-XANES with low baseline (280-283 eV region) and
308 high absorption at ~292 eV (Fig. 5c). On the other hand, ROI#2 and ROI#4 are diffused OM as seen
309 by C-map (Fig. 5b) as well as C-XANES with higher baseline and lower absorption at ~292 eV due
310 to lower concentration of carbon (Fig. 5c). Note that the FIB section of AhS 91A did not contain
311 detectable amount of carbon, likely due to the large heterogeneity in micrometer scale of AhS 91A.
312 Therefore, we focused on AhS 671 for further nanoscale analysis.
313



315 Fig. 5: (a) STXM elemental map of the FIB section from AhS 671. (b) STXM C-map with ROIs. (c)
316 C-XANES spectra from ROIs shown in (b).

317
318 To compare the molecular structures of each area, we obtained the peak intensities at 285.0 eV
319 (aromatic/olefinic C), 287.5 eV (aliphatic C), and 288.7 eV [C(=O)O] by subtracting a linear
320 baseline and normalizing to the intensities at 291.5 eV (approximately at ionization potential energy)
321 (Fig. 6). It should be noted that functional group abundances in Fig. 6 are not exact fractions in OM,
322 but rather the ratios are relative indicators to compare molecular structure heterogeneity among the
323 regions. These diagrams showed that ROI#1 (condensed OM) was highly aromatic in nature, and
324 ROIs #2 and #4 (diffused OM) were less aromatic in nature. This tendency is consistent with OM in

325 type 1 and 2 chondrites (Le Guillou et al. 2014), but overall AhS 671 is richer in aromatics than type
 326 1 and 2 chondrites. ROI#3 plotted off from the trends and was rich in C(=O)O and aliphatic C.
 327



329 Fig. 6: C-XANES peak intensity ratios of AhS 671. The data from ROIs in Fig. 5 is indicated by
 330 color, and gray circle represents data from other regions in the FIB section.

331

332 The OM grains were distributed in the Fe-rich matrix (Fig. 5a). The Fe-XANES spectra in these
 333 regions (ROI#2 and ROI#4 in Fig. 5b) were consistent with phyllosilicates (see next section) (Fig.
 334 7c). Fe²⁺ rich regions were clearly distinguished in the AhS 671 FIB section (green in Fig. 7a) and
 335 were likely olivine (Fig. 8), but no/little OM were found in these regions.

336

337 Using the method of Le Guillou et al. (2015) which is modified from Bourdelle et al. (2013), the
 338 Fe³⁺/ΣFe values in silicates could be calculated by the peak intensity ratios of $R_{L3} = I_{Fe^{3+}}/I_{total}$ using
 339 the integrated peak intensities of the Fe L₃ edge at 707.6-710.8 eV as $I_{Fe^{3+}}$ and 704-711 eV as I_{total} ;

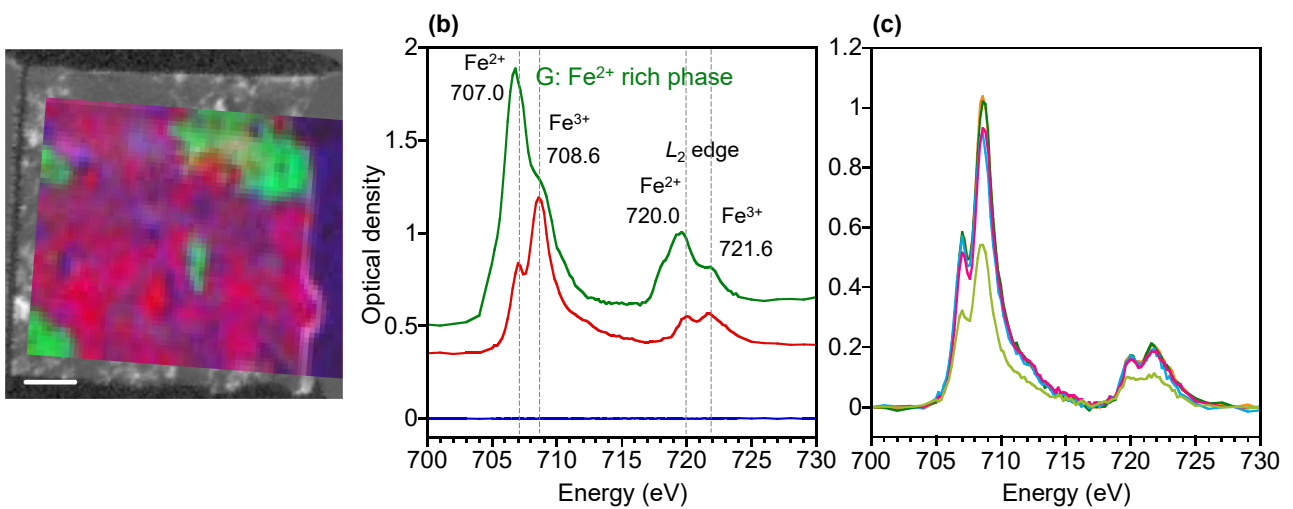
$$340 \quad \frac{Fe^{3+}}{\Sigma Fe} = \frac{R_{L3} - 0.2614}{0.006} \% \quad (\text{eq. 1})$$

341 The average Fe³⁺/ΣFe ratio at ROI#2 and ROI#4 was 74.9±2.7 %. This value is slightly higher than
 342 the values of silicates in CR2 chondrites (66-75%) and CM chondrites (50-70%) (Le Guillou et al.
 343 2015 and references therein). While, employing the method of van Aken and Liescher (2002) which
 344 could be more universal, the Fe³⁺/ΣFe values were calculated with;

345
$$\frac{I_{L3}}{I_{L2}} = \frac{1}{ax^2+bx+x} - 1 \quad (\text{eq. 2})$$

346 where I_{L3} is the integrated intensity of Fe^{3+} L_3 edge (707.6-709.6 eV), I_{L2} is the integrated
 347 intensity of Fe^{2+} L_2 edge (719.0-721.0 eV), $a = 0.193$, $b = -0.465$, $c = 0.366$, and $x = \text{Fe}^{3+}/\Sigma\text{Fe}$. With
 348 this method, the average $\text{Fe}^{3+}/\Sigma\text{Fe}$ ratio at ROI#2 and ROI#4 was 60.3 ± 4.2 %. This ratio is lower
 349 than the previous one, but likely closer to the actual $\text{Fe}^{3+}/\Sigma\text{Fe}$ ratio in the sample. A calibration is
 350 required to obtain the precise ratios, but it is beyond the scope of our study.

351



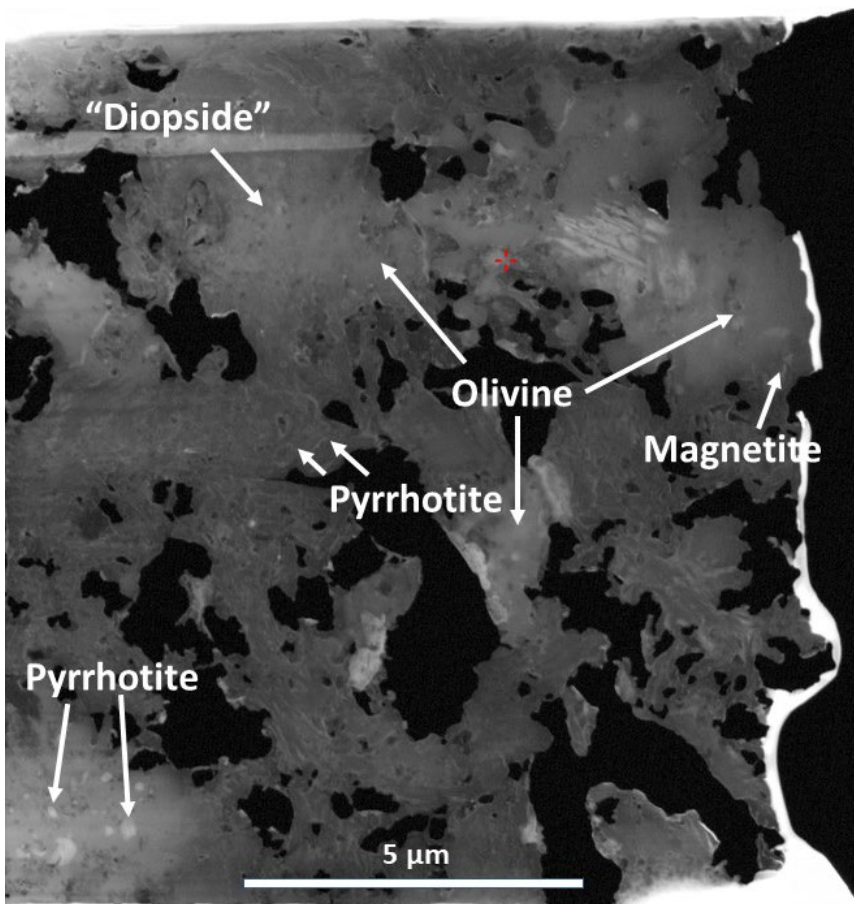
352

357

358 Mineralogy

359 Fig. 8 shows the results of transmission Kikuchi diffraction (TKD) of the FIB slice of AhS 671
 360 featured in this current paper. We identified the following crystalline phases: olivine, pyrrhotite and
 361 magnetite. Based on EDS compositions, and comparison with TEM imaging of AhS 91A (Goodrich
 362 et al. 2019) the bulk of this FIB slice consists of poorly-crystalline serpentine and saponite. One area
 363 of the FIB slice produced multiple TKD patterns for diopside. These were all individual,

364 unconnected pixels, which must be viewed with caution. However, these were the only diopside
365 diffraction matches in the FIB slice, and this area produced only matches to this phase. Therefore, the
366 phases might actually be diopside. Comparison with Fig. 5 indicates that the O-rich areas in that
367 figure contain well-crystalline olivine and possibly diopside, while the Fe-rich areas are poorly
368 crystalline, representing the poorly-crystalline phyllosilicates observed in Goodrich et al. (2019).
369



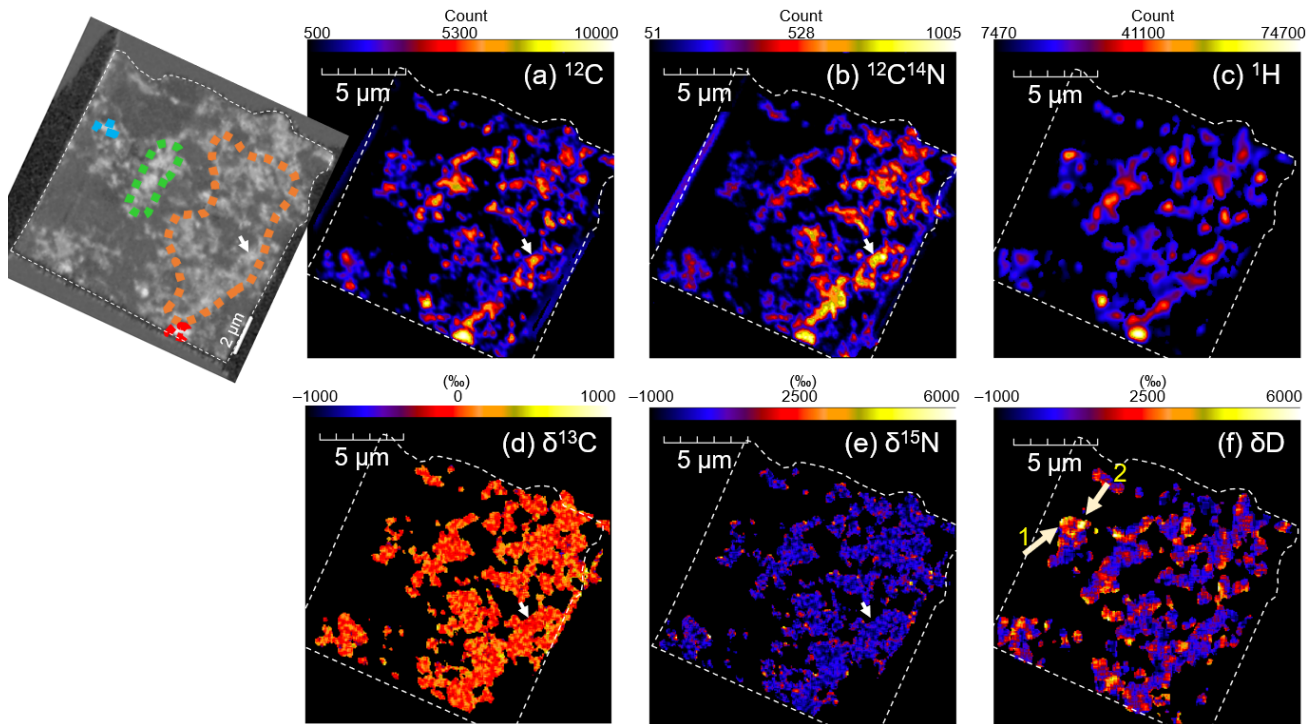
371 Fig. 8: Crystalline phases identified in the FIB slice of AhS 671 by TKD, shown on a BSE image.
372 Phase identified as "Diopside" is a tentative identification.

373

374 NanoSIMS

375 δD , $\delta^{15}N$, and $\delta^{13}C$ values of AhS 671 obtained by NanoSIMS are shown in Table 3 and Fig. 1b-d,
376 and elemental and isotope images are shown in Fig. 9. The average δD value of the C-rich area was
377 approximately +1000‰, with some isotopic "hot spots" up to approximately +4000‰. The average

378 $\delta^{15}\text{N}$ and $\delta^{13}\text{C}$ values of the C-rich area were approximately +100 to +200‰ and -5 to +3‰,
 379 respectively. An $\delta^{13}\text{C}$ anomalous area was observed with $\delta^{13}\text{C}$ values of -132 ± 26 ‰. The C-XANES
 380 characteristics of these hot spots and the $\delta^{13}\text{C}$ anomalous area did not show significant differences
 381 from surrounding OM.
 382



384 Fig. 9: NanoSIMS elemental and isotopic composition images of AhS 671. (a) ^{12}C , (b) $^{12}\text{C}^{14}\text{N}$, (c)
 385 ^1H , (d) $\delta^{13}\text{C}$, (e) $\delta^{15}\text{N}$, and (f) δD . Arrows in (a, b, d, e) indicate a $\delta^{13}\text{C}$ anomalous spot. Arrows in (f)
 386 indicate δD hot spots.

387

388 Table 3. $\delta^{13}\text{C}$, $\delta^{15}\text{N}$, and δD values obtained from the FIB section of AhS 671 by NanoSIMS.

AhS 671		$\delta^{13}\text{C}$ ‰	$\delta^{15}\text{N}$ ‰	δD ‰
Run#1	Entire	-4.5 ±4.1	+283 ±59	
	C-rich area	-5.4 ±6.2	+121 ±30	
Run#2	Entire	+2.9 ±3.4	+648 ±44	
	C-rich area	+3.1 ±3.3	+234 ±32	
	C anomalous area	-132 ±26	-361 ±239	
Run#3	C-rich area			+988 ±59

Hot spot #1	+2087 ±695
Hot spot #2	+4246 ±1430

389 Errors are standard deviation (1σ).

390 Entire: entire area analyzed, C-rich area: carbon-rich regions chosen by distributions of ^{12}C within a
391 section applying 10% threshold of total ^{12}C ion counts, and C anomalous area: a $\delta^{13}\text{C}$ anomalous spot
392 shown in Fig. 9.

393

394 **DISCUSSION**

395 **Elemental and Isotopic Characteristics**

396 Elemental and isotopic characteristics of OM reflect degrees of alteration and metamorphism, and
397 thus these characteristics can be used to evaluate its origin as well as for classification of its host
398 meteorite (Alexander et al. 2007; Alexander et al. 2010). In summary, the elemental and isotopic
399 compositions of AhS 671 are similar to those of diverse CCs, but do not exactly match with any
400 known groups. High abundances of bulk C with moderate N/C ratios in AhS 671 compared to
401 various chondrites, were close to the values of CI chondrites and Tagish Lake (Alexander et al. 2012)
402 (Fig. 1a). However, the bulk $\delta^{13}\text{C}$ of AhS 671 was rather close to CM and CR chondrites, while $\delta^{15}\text{N}$
403 is consistent with CI, CM, and Tagish Lake (Alexander et al. 2012) (Fig. 1c). The NanoSIMS
404 analysis allows us to obtain microscale $\delta^{13}\text{C}$, $\delta^{15}\text{N}$, and δD values on C-rich areas (most likely
405 organics) in AhS 671. The $\delta^{13}\text{C}$ values of the C-rich areas and the entire areas were consistent with
406 the bulk AhS 671 value. However, the $\delta^{15}\text{N}$ values of the C-rich areas were higher than the bulk
407 value and close to CR chondrites (Alexander et al. 2012), and the entire areas were even higher than
408 the C-rich areas (up to ~650‰) (Fig. 1b, c). The differences in the $\delta^{15}\text{N}$ among bulk and NanoSIMS
409 entire and C-rich areas could be due to local heterogeneities of N-compounds and/or the presence of
410 inorganic N-bearing compounds. The δD values of C-rich areas in AhS 671 were similar to the IOM
411 from CI, CM, and Tagish Lake (Alexander et al. 2007; Alexander et al. 2010; Herd et al. 2011), but
412 much higher if compared to the values of bulk chondrites (Alexander et al. 2012) (Fig. 1d).

413

414 The elemental and isotopic compositions of AhS 91A fragments showed large heterogeneity. In
415 general, C and N abundances were lower than in AhS 671 (Table 1 and Fig. 1a). The $\delta^{13}\text{C}$ of AhS
416 91A was slightly lower than AhS 671, the $\delta^{15}\text{N}$ could be higher than AhS 671, although we could
417 obtain the $\delta^{15}\text{N}$ values from only a single fragment of AhS 91A due to the small sample size (<100
418 ng of N) (Table 1 and Fig. 1b,c). Loss of C and N could be explained by the thermal processing, but
419 differences in $\delta^{15}\text{N}$ between AhS 671 and AhS 91A rather indicate differences in origin of OM. The
420 elemental and isotopic compositions of both AhS 671 and AhS 91A are clearly distinguished from
421 those ureilitic lithologies of AhS (Downes et al. 2015) (Fig. 1), consistent with the fact that AhS 671
422 and AhS 91A are xenoliths and the amount of ureilitic material in these lithologies is small (Goodrich
423 et al. 2019).

424

425 **Molecular Structures of Organic Matter in AhS 671 and AhS 91A**

426 The infrared spectra of AhS 671 and AhS 91A showed that OM—at least aliphatic-containing OM—
427 was not very abundant, and such bulk IR features were consistent with local observation by C-
428 XANES. The small aliphatic C-H peaks and their relatively high CH_2/CH_3 peak intensity ratios were
429 similar to IR characteristics of type 3 chondrites such as Kaba (CV3.0/3.1) (Kebukawa et al. 2011;
430 Kebukawa et al. 2019a) and heated CM chondrites (Quirico et al. 2018).

431

432 Raman D and G band parameters are a good indicator for degree of thermal processing of
433 macromolecular OM. The Raman parameters of both AhS 671 and AhS 91A were somewhat unique
434 among chondrites (Fig. 4). The D band parameters (Γ_{D} and ω_{D}) of AhS 671 indicate slight heating,
435 while the G band parameters plotted in the opposite direction to the heating trend (Fig. 4a,b). The D
436 band parameters of AhS 91A were also indicative of slight heating. The Γ_{G} and $I_{\text{D}}/I_{\text{G}}$ values of AhS
437 91A were close to type 2 chondrites (Tagish Lake, Murchison, and Y-793321), but the ω_{G} was close
438 to thermally metamorphosed type 3 CCs (Allende and Moss) (Fig. 4b,d). Such mixed Raman

439 features are likely due to highly aromatic but not graphene-like structures. It is consistent with the C-
440 XANES spectra which show high aromatic content but not the $1s\text{-}\sigma^*$ exciton peak at 291.7 eV due to
441 graphene structures (Cody et al. 2008). These trends were somewhat similar to the experimentally-
442 heated Tagish Lake and Murchison meteorites (Chan et al. 2019; Kiryu et al. 2020). The high Γ_G
443 values of AhS 671 and AhS 91A could be explained by an increase in development in the sizes of
444 crystalline domains without graphitic ordering (Chan et al. 2019). These Raman characteristics are
445 indicative of short-term heating—possibly by impact.

446

447 Some of the ureilitic stones from AhS contain disordered carbonaceous compounds as well as
448 crystalline graphite and diamond (Jenniskens et al. 2009; Kaliwoda et al. 2013). Kaliwoda et al.
449 (2013) showed zones which consist of different carbon phases and large areas with disordered
450 graphitic material, accompanied with some tiny patches of crystalline graphite as revealed by Raman
451 mapping analysis. Although no genetic relationship is suspected between the carbonaceous materials
452 in ureilitic lithologies and those in AhS 671 and AhS 91A, the Raman spectrum of the most
453 “disordered” phase in Kaliwoda et al. (2013) is similar to our AhS 671 spectra.

454

455 Local heterogeneity of OM in the micron to submicrometer scale is observed in AhS 671 by
456 STXM/C-XANES. In general, globule-like or compacted OM shows more aromatic nature, and
457 diffused OM is less aromatic and contains more O-bearing functional groups. These trends are
458 consistent with type 1 and 2 chondrites, and soluble OM may contribute to diffuse OM (Le Guillou
459 et al. 2014). The C-XANES spectra of AhS 671 are characterized by fewer aliphatic and O-bearing
460 functional groups compared to type 1 and 2 chondrites (Le Guillou et al. 2014), and these
461 characteristics are consistent with mild heating perhaps by impact processing.

462

463 The OM-rich area (e.g., ROI#4 in Fig. 5) was also rich in Fe^{3+} (Fig. 7) and this region likely
464 consisted poorly-crystalline phyllosilicates. The associations of OM with phyllosilicates or

465 amorphous silicates were well known for CCs in submicrometer scale (Abreu and Brearley 2010;
466 Changela et al. 2018; Le Guillou et al. 2014; Le Guillou and Brearley 2014; Vinogradoff et al. 2017;
467 Vollmer et al. 2014). The $\text{Fe}^{3+}/\Sigma\text{Fe}$ ratios in this region were slightly higher than the values of
468 silicates in type 2 chondrites (Le Guillou et al. 2015 and references therein). Since decreases in Fe^{3+}
469 indicate progressive alteration due to the transfer of Fe^{3+} from silicates to oxides (Le Guillou et al.
470 2015), the OM rich areas in AhS 671 may not have been subjected to progressive aqueous alteration.

471

472 **Comparison between AhS 671 and carbonaceous chondritic clasts in various meteorites**

473 Overall, our analyses of AhS 671 are consistent with a C1 lithology but distinguished from known
474 groups of CCs, as discussed by Goodrich et al. (2019). Goodrich et al. (2019) discussed comparisons
475 between this lithology and other known xenolithic CC-like clasts in brecciated meteorites. Thus, we
476 extend that comparison using our data for AhS 671.

477

478 Visser et al. (2018) estimated peak metamorphic temperatures of 30 volatile-rich clasts (16 CI-, and
479 14 CM-like clasts) in 10 different host meteorites (4 polymict ureilites, 5 polymict eucrites, and 1
480 howardite) by Raman carbon thermometry. They showed that the peak temperatures experienced by
481 CI-like clasts and CM-like clasts ranged between 30–110 °C with an average of 65 ± 25 °C, and
482 between 50–110 °C with an average of 70 ± 25 °C, respectively, indicating that they had not
483 experienced peak temperatures higher than typical CM and CI chondrites. On the other hand, our
484 Raman investigations of AhS 671 indicated slight heating somewhat similar to insoluble organic
485 matter (IOM) from Y-86720, a heated CM chondrite with the heating stage of IV (>750 °C)
486 (Nakamura 2005), whose Raman parameters were $\omega_D = 1348.6 \pm 0.3 \text{ cm}^{-1}$, $\Gamma_D = 244.7 \pm 0.5 \text{ cm}^{-1}$, $\omega_G =$
487 $1583.4 \pm 0.3 \text{ cm}^{-1}$, $\Gamma_D = 96.0 \pm 0.2 \text{ cm}^{-1}$, and $I_D/I_G = 1.16 \pm 0.05$ (Busemann et al. 2007). Note that our
488 Raman D and G band parameters are comparable to those in Busemann et al. (2007) but not to those
489 in Visser et al. (2018) due to the difference in the fitting methods employed (Kiryu et al. 2020).

490

491 Patzek et al. (2020) reported that δD values of CI-like clasts in polymict ureilites (DaG 319, DaG
492 999, and EET 83309) range from +950 to +3100‰, and those in CR chondrites (Al Rais and
493 Renazzo) have δD values from +740 to +2480‰ (Fig. 1d), while CI-like clasts in NWA 7542 (an
494 HED meteorite) have δD values from +200 to +640‰, and δD in a CI-like clast in the ordinary
495 chondrite Sahara 98645 ranges from -290 to +270‰. δD values of five CM-like clasts in the HED
496 meteorites (NWA 7542, Sariççek, and EET 87513) range from -220 to +340‰ (Patzek et al. 2020).
497 The δD of AhS 671 is ~1000‰ and in the range of CI-like clasts in polymict ureilites and in CR
498 chondrites (Fig. 1d). The OM in clasts in DaG 999 have a primitive nature as shown by Raman
499 parameters with estimated peak metamorphic temperatures of less than 100 °C (Visser et al. 2018),
500 and thus at least the clasts in DaG 999 are distinguished from AhS 671.

501

502 The Zag meteorite (an H3-6 ordinary chondrite) hosts a unique CC-like clast likely originating from
503 a primitive body such as D/P asteroids (Kebukawa et al. 2019b; Kebukawa et al. 2020; Zolensky et
504 al. 2017), as well as xenolithic halite particles, some included within the CC clast (Chan et al. 2018;
505 Rubin et al. 2002). Compared to the CC-like clast in the Zag meteorite, C, N, H-isotopic
506 characteristics of AhS 671 are not very close (Fig. 1). The C-XANES features of AhS 671 (Fig. 5c)
507 are somewhat similar to the C-rich aggregate in the Zag clast (Kebukawa et al. 2019b), but not
508 similar to other OM phases in the Zag clast (Kebukawa et al. 2020). C-rich aggregates were found in
509 a type 3 ordinary chondrite, Sharps (Brearley 1990), but their C-XANES characteristics are rather
510 graphitic (Kebukawa et al. 2017), and thus well distinguished from AhS 671. On the other hand, a
511 carbon rich clast in a CR2 chondrite, LaPaz Icefield 02342, is rich in O-bearing functional groups in
512 C-XANES with the average values of $\delta D \approx +130\text{‰}$ and $\delta^{15}\text{N} \approx 0\text{‰}$ (Nittler et al. 2019), and these
513 characteristics are distinguished from AhS 671.

514

515 Overall, AhS 671 shows some similarities to, but does not exactly match any known CC-like clasts,
516 although there are not enough data for a full comparison. As suggested by Patzek et al. (2020), the

517 C1 clasts in several meteorite groups prove the existence of additional primitive, volatile-rich
518 material in the early Solar System, besides the samples available as the CI, CM, and CR chondrites.
519 The C1-lithologies of AhS support the idea that there are much larger diversities in the CC parent
520 bodies than these we already sampled.

521

522 **Implications for Origin of AhS CC-lithologies**

523 As described in detail by Goodrich et al. (2019), AhS 91A and AhS 671 are dominated by a hydrous
524 CC lithology consisting of fine-grained phyllosilicates (serpentine and saponite) and amorphous
525 material, magnetite, bruennerite, dolomite, olivine (Fo 28-42), an unidentified Ca-rich silicate phase,
526 pyrrhotite, pentlandite, Ca-phosphate and ilmenite. The mineralogy we determined from the FIB of
527 AhS 671 is consistent with the previous work, except for our still tentative identification of diopside.
528 These stones have obvious mineralogic similarities to CI1 chondrites, but the Ca-rich silicate
529 (tentatively identified as consisting mainly of dehydrated saponite) and magnetite-fayalite
530 assemblages indicate heterogeneous post-aqueous alteration thermal metamorphism. The bulk
531 oxygen isotope composition of AhS 91A ($\delta^{18}\text{O} = 13.53\text{‰}$, $\delta^{17}\text{O} = 8.93\text{‰}$) is unlike that of any
532 known CC, but is essentially identical to that of a C1 clast in the Nilpena polymict ureilite (Goodrich
533 et al. 2019).

534

535 Goodrich et al. (2019) suggested that AhS 671 and AhS 91A were likely derived from the same
536 original carbonaceous chondritic parent body, but that they experienced different degrees of thermal
537 processing, higher in AhS 671 than in AhS 91A. Our organic analyses of these lithologies are
538 generally consistent with this idea, but suggest that the degree of thermal processing is actually
539 higher in AhS 91A than in AhS 671 as indicated by C abundances. Such an inconsistency could be
540 due to sample heterogeneity, as we see large heterogeneities in elemental and isotopic analysis in
541 AhS 91A (Fig. 1a). Our analyses of OM molecular structures showed evidence of slight heating,
542 likely short-term heating possibly by impact, rather than long-term thermal metamorphism induced

543 by decay of radioactive nuclides. Such impact heating could have occurred at the original parent
544 body of AhS 671 and AhS 91A, rather than at the time of implantation into the ureilitic parent body.
545 However, there are some differences between AhS 671 and AhS 91A which cannot be explained only
546 by different degrees of heating. There were likely at least two reservoirs of OM as indicated by
547 isotopic signatures (see Discussion, Elemental and Isotopic Characteristics).

548

549 **CONCLUSIONS**

550 Organic matter in the xenolithic carbonaceous chondritic lithologies of Almahata Sitta (AhS), AhS
551 671 and AhS 91A showed unique features indicating that they represent CC-like material not
552 previously sampled in our meteorite collection:

553

554 1. Elemental and isotopic analyses of AhS 671 and AhS 91A indicate primitive, outer Solar System
555 origin of their parent body, and there were likely at least two reservoirs of OM.

556

557 2. Raman D and G band parameters of AhS 671 and AhS 91A indicate slight heating, likely short-
558 term heating possibly by impact, rather than long-term thermal metamorphism induced by decay of
559 radioactive nuclides.

560

561 3. The small aliphatic C-H peaks of AhS 671 and AhS 91A in the IR spectra and their relatively high
562 CH₂/CH₃ peak intensity ratios were similar to type 3 chondrites and heated CM chondrites. The C-
563 XANES spectra of AhS 671 are characterized by fewer aliphatic and O-bearing functional groups as
564 compared to primitive type 1 and 2 chondrites. These IR and C-XANES features are consistent with
565 mild heating perhaps by impact induced heating process.

566

567 4. C1-lithologies of AhS support the idea that there are much larger diversities in primitive
568 carbonaceous chondritic materials in the Solar System than those we have already sampled.

569

570 **Acknowledgements**

571 We thank the Associated Editor Scott Sandford and an anonymous reviewer for their fruitful
572 comments. This work was supported by JSPS KAKENHI (grant numbers JP17H06458,
573 JP18K03722, and JP19H05073). The operations of the Advanced Light Source are supported by the
574 Director, Office of Science, Office of Basic Energy Sciences, US Department of Energy under
575 Contract No. DE-AC02-05CH11231. MZ and JM were supported by the NASA Emerging Worlds
576 Program.

577

578 **References**

- 579 Abreu N. M. and Brearley A. J. 2010. Early solar system processes recorded in the matrices of two
580 highly pristine CR3 carbonaceous chondrites, MET 00426 and QUE 99177. *Geochimica et*
581 *Cosmochimica Acta* 74:1146-1171.
- 582 Alexander C. M. O. D., Bowden R., Fogel M. L., Howard K. T., Herd C. D., and Nittler L. R. 2012.
583 The provenances of asteroids, and their contributions to the volatile inventories of the terrestrial
584 planets. *Science* 337:721-723.
- 585 Alexander C. M. O. D., Fogel M., Yabuta H., and Cody G. D. 2007. The origin and evolution of
586 chondrites recorded in the elemental and isotopic compositions of their macromolecular
587 organic matter. *Geochimica et Cosmochimica Acta* 71:4380-4403.
- 588 Alexander C. M. O. D., Newsome S. D., Fogel M. L., Nittler L. R., Busemann H., and Cody G. D.
589 2010. Deuterium enrichments in chondritic macromolecular material—Implications for the
590 origin and evolution of organics, water and asteroids. *Geochimica et Cosmochimica Acta*
591 74:4417-4437.
- 592 Bourdelle F., Benzerara K., Beyssac O., Cosmidis J., Neuville D. R., Brown G. E., and Paineau E.
593 2013. Quantification of the ferric/ferrous iron ratio in silicates by scanning transmission X-ray
594 microscopy at the Fe L_{2,3} edges. *Contributions to Mineralogy and Petrology* 166:423-434.
- 595 Brearley A. J. 1990. Carbon-rich aggregates in type 3 ordinary chondrites: Characterization, origins,
596 and thermal history. *Geochimica et Cosmochimica Acta* 54:831-850.
- 597 Busemann H., Alexander C. M. O. D., and Nittler L. R. 2007. Characterization of insoluble organic
598 matter in primitive meteorites by microRaman spectroscopy. *Meteoritics & Planetary Science*
599 42:1387-1416.
- 600 Busemann H., Young A. F., Alexander C. M. O., Hoppe P., Mukhopadhyay S., and Nittler L. R. 2006.
601 Interstellar chemistry recorded in organic matter from primitive meteorites. *Science* 312:727-

602
603
604
605
606
607
608
609
610
611
612
613
614
615
616
617
618
619
620
621
622
623
624
625
626
627
628
629
630
631
632
633
634
635
636
637
638
639

730.

- Chan Q. H. S., Nakato A., Kebukawa Y., Zolensky M. E., Nakamura T., Maisano J. A., Colbert M. W., Martinez J. E., Kilcoyne A. L. D., Suga H., Takahashi Y., Takeichi Y., Mase K., and Wright I. P. 2019. Heating experiments of the Tagish Lake meteorite: Investigation of the effects of short-term heating on chondritic organics. *Meteoritics & Planetary Science* 54:104-125.
- Chan Q. H. S., Zolensky M. E., Kebukawa Y., Fries M., Ito M., Steele A., Rahman Z., Nakato A., Kilcoyne A. L. D., Suga H., Takahashi Y., Takeichi Y., and Mase K. 2018. Organic matter in extraterrestrial water-bearing salt crystals. *Science advances* 4:eao3521.
- Changela H. G., Le Guillou C., Bernard S., and Brearley A. J. 2018. Hydrothermal evolution of the morphology, molecular composition, and distribution of organic matter in CR (Renazzo-type) chondrites. *Meteoritics & Planetary Science* 53:1006-1029.
- Cody G. D., Alexander C. M. O. D., Yabuta H., Kilcoyne A. L. D., Araki T., Ade H., Dera R., Fogel M., Militzer B., and Mysen B. O. 2008. Organic thermometry for chondritic parent bodies. *Earth and Planetary Science Letters* 272:446-455.
- Collinet M. and Grove T. L. 2020. Incremental melting in the ureilite parent body: Initial composition, melting temperatures, and melt compositions. *Meteoritics & Planetary Science* 55:832-856.
- Downes H., Abernethy F. A. J., Smith C. L., Ross A. J., Verchovsky A. B., Grady M. M., Jenniskens P., and Shaddad M. H. 2015. Isotopic composition of carbon and nitrogen in ureilitic fragments of the Almahata Sitta meteorite. *Meteoritics & Planetary Science* 50:255-272.
- Ferrari A. C. and Robertson J. 2000. Interpretation of Raman spectra of disordered and amorphous carbon. *Physical Review B* 61:14095-14107.
- Goodrich C. A., Hartmann W. K., O'Brien D. P., Weidenschilling S. J., Wilson L., Michel P., and Jutzi M. 2015. Origin and history of ureilitic material in the solar system: The view from asteroid 2008 TC 3 and the Almahata Sitta meteorite. *Meteoritics & Planetary Science* 50:782-809.
- Goodrich C. A., Van Orman J. A., and Wilson L. 2007. Fractional melting and smelting on the ureilite parent body. *Geochimica et Cosmochimica Acta* 71:2876-2895.
- Goodrich C. A., Zolensky M. E., Fioretti A. M., Shaddad M. H., Downes H., Hiroi T., Kohl I., Young E. D., Kita N. T., Hamilton V. E., Riebe M. E. I., Busemann H., Macke R. J., Fries M., Ross D. K., and Jenniskens P. 2019. The first samples from Almahata Sitta showing contacts between ureilitic and chondritic lithologies: Implications for the structure and composition of asteroid 2008 TC3. *Meteoritics & Planetary Science* 54:2769-2813.
- Hashiguchi M., Kobayashi S., and Yurimoto H. 2015. Deuterium- and ¹⁵N-signatures of organic globules in Murchison and Northwest Africa 801 meteorites. *Geochemical Journal* 49:377-391.
- Herd C. D. K., Blinova A., Simkus D. N., Huang Y., Tarozo R., Alexander C. M. O. D., Gyngard F., Nittler L. R., Cody G. D., Fogel M. L., Kebukawa Y., Kilcoyne A. L. D., Hilts R. W., Slater G. F., Glavin D. P., Dworkin J. P., Callahan M. P., Elsila J. E., De Gregorio B. T., and Stroud R. M. 2011. Origin and evolution of prebiotic organic matter as inferred from the Tagish Lake meteorite. *Science* 332:1304-1307.

640 Isaji Y., Ogawa N. O., Boreham C. J., Kashiyama Y., and Ohkouchi N. 2020. Evaluation of $\delta^{13}\text{C}$ and
641 $\delta^{15}\text{N}$ Uncertainties Associated with the Compound-Specific Isotope Analysis of
642 Geoporphyrins. *Analytical Chemistry* 92:3152-3160.

643 Ito M. and Messenger S. 2008. Isotopic imaging of refractory inclusions in meteorites with the
644 NanoSIMS 50L. *Applied Surface Science* 255:1446-1450.

645 Ito M., Uesugi M., Naraoka H., Yabuta H., Kitajima F., Mita H., Takano Y., Karouji Y., Yada T.,
646 Ishibashi Y., Okada T., and Abe M. 2014. H, C, and N isotopic compositions of Hayabusa
647 category 3 organic samples. *Earth, Planets and Space* 66:91.

648 Jenniskens P., Shaddad M. H., Numan D., Elsir S., Kudoda A. M., Zolensky M. E., Le L., Robinson
649 G. A., Friedrich J. M., Rumble D., Steele A., Chesley S. R., Fitzsimmons A., Duddy S., Hsieh
650 H. H., Ramsay G., Brown P. G., Edwards W. N., Tagliaferri E., Boslough M. B., Spalding R.
651 E., Dantowitz R., Kozubal M., Pravec P., Borovicka J., Charvat Z., Vaubaillon J., Kuiper J.,
652 Albers J., Bishop J. L., Mancinelli R. L., Sandford S. A., Milam S. N., Nuevo M., and Worden
653 S. P. 2009. The impact and recovery of asteroid 2008 TC3. *Nature* 458:485-488.

654 Kaliwoda M., Hochleitner R., Hoffmann V. H., Mikouchi T., Gigler A. M., and Schmahl W. W. 2013.
655 New Raman Spectroscopic Data of the Almahata Sitta Meteorite. *Spectroscopy Letters* 46:141-
656 146.

657 Kebukawa Y., Alexander C. M. O. D., and Cody G. D. 2011. Compositional diversity in insoluble
658 organic matter in type 1, 2 and 3 chondrites as detected by infrared spectroscopy. *Geochimica
659 et Cosmochimica Acta* 75:3530-3541.

660 Kebukawa Y., Alexander C. M. O. D., and Cody G. D. 2019a. Comparison of FT - IR spectra of bulk
661 and acid insoluble organic matter in chondritic meteorites: An implication for missing carbon
662 during demineralization. *Meteoritics & Planetary Science* 54:1632-1641.

663 Kebukawa Y., Ito M., Zolensky M. E., Greenwood R. C., Rahman Z., Suga H., Nakato A., Chan Q. H.,
664 Fries M., and Takeichi Y. 2019b. A novel organic-rich meteoritic clast from the outer solar
665 system. *Scientific reports* 9:3169.

666 Kebukawa Y., Nakashima S., and Zolensky M. E. 2010. Kinetics of organic matter degradation in the
667 Murchison meteorite for the evaluation of parent-body temperature history. *Meteoritics &
668 Planetary Science* 45:99-113.

669 Kebukawa Y., Zolensky M. E., Chan Q. H. S., Nagao K., Kilcoyne A. L. D., Bodnar R. J., Farley C.,
670 Rahman Z., Le L., and Cody G. D. 2017. Characterization of carbonaceous matter in xenolithic
671 clasts from the Sharps (H3.4) meteorite: Constraints on the origin and thermal processing.
672 *Geochimica et Cosmochimica Acta* 196:74-101.

673 Kebukawa Y., Zolensky M. E., Ito M., Ogawa N. O., Takano Y., Ohkouchi N., Nakato A., Suga H.,
674 Takeichi Y., Takahashi Y., and Kobayashi K. 2020. Primordial organic matter in the xenolithic
675 clast in the Zag H chondrite: Possible relation to D/P asteroids. *Geochimica et Cosmochimica
676 Acta* 271:61-77.

677 Kilcoyne A., Tyliszczak T., Steele W., Fakra S., Hitchcock P., Franck K., Anderson E., Harteneck B.,

678 Rightor E., and Mitchell G. 2003. Interferometer-controlled scanning transmission X-ray
679 microscopes at the Advanced Light Source. *Journal of synchrotron radiation* 10:125-136.

680 Kiryu K., Kebukawa Y., Igisu M., Shibuya T., Zolensky M. E., and Kobayashi K. 2020. Kinetics in
681 thermal evolution of Raman spectra of chondritic organic matter to evaluate thermal history of
682 their parent bodies. *Meteoritics & Planetary Science* in press.

683 Koprinarov I. N., Hitchcock A. P., McCrory C. T., and Childs R. F. 2002. Quantitative Mapping of
684 Structured Polymeric Systems Using Singular Value Decomposition Analysis of Soft X-ray
685 Images. *The Journal of Physical Chemistry B* 106:5358-5364.

686 Le Guillou C., Bernard S., Brearley A. J., and Remusat L. 2014. Evolution of organic matter in Orgueil,
687 Murchison and Renazzo during parent body aqueous alteration: In situ investigations.
688 *Geochimica et Cosmochimica Acta* 131:368-392.

689 Le Guillou C. and Brearley A. 2014. Relationships between organics, water and early stages of aqueous
690 alteration in the pristine CR3.0 chondrite MET 00426. *Geochimica et Cosmochimica Acta*
691 131:344-367.

692 Le Guillou C., Changela H. G., and Brearley A. J. 2015. Widespread oxidized and hydrated amorphous
693 silicates in CR chondrites matrices: Implications for alteration conditions and H₂ degassing of
694 asteroids. *Earth and Planetary Science Letters* 420:162-173.

695 Mittlefehldt D. W., McCoy T. J., Goodrich C. A., and Kracher A. 1998. Non-chondritic meteorites
696 from asteroidal bodies. In *Planetary materials* (ed. J. J. Papike), pp. 4-1–4-195. Mineralogical
697 Society of America, Washington, D.C.

698 Nakamura T. 2005. Post-hydration thermal metamorphism of carbonaceous chondrites. *Journal of*
699 *Mineralogical and Petrological Sciences* 100:260-272.

700 Nittler L. R., Stroud R. M., Trigo-Rodríguez J. M., De Gregorio B. T., Alexander C. M. O. D.,
701 Davidson J., Moyano-Camero C. E., and Tanbakouei S. 2019. A cometary building block in a
702 primitive asteroidal meteorite. *Nature Astronomy* 3:659-666.

703 Ogawa N. O., Nagata T., Kitazato H., and Ohkouchi N. 2010. Ultra sensitive elemental
704 analyzer/isotope ratio mass spectrometer for stable nitrogen and carbon isotope analyses. In
705 *Earth, life, and isotopes* (eds. N. Ohkouchi, I. Tayasu, and K. Koba), pp. 339-353. Kyoto
706 University Press.

707 Orthous-Daunay F.-R., Piani L., Flandinet L., Thissen R., Wolters C., Vuitton V., Poch O., Moynier F.,
708 Sugawara I., and Naraoka H. 2019. Ultraviolet-photon fingerprints on chondritic large organic
709 molecules. *Geochemical Journal* 53:21-32.

710 Patzek M., Hoppe P., Bischoff A., Visser R., and John T. 2020. Hydrogen isotopic composition of CI-
711 and CM-like clasts from meteorite breccias – Sampling unknown sources of carbonaceous
712 chondrite materials. *Geochimica et Cosmochimica Acta* 272:177-197.

713 Prince K. C., Avaldi L., Coreno M., Camilloni R., and Simone M. d. 1999. Vibrational structure of
714 core to Rydberg state excitations of carbon dioxide and dinitrogen oxide. *Journal of Physics B:*
715 *Atomic, Molecular and Optical Physics* 32:2551-2567.

716 Quirico E., Bonal L., Beck P., Alexander C. M. O. D., Yabuta H., Nakamura T., Nakato A., Flandinet
717 L., Montagnac G., Schmitt-Kopplin P., and Herd C. D. K. 2018. Prevalence and nature of
718 heating processes in CM and C2-ungrouped chondrites as revealed by insoluble organic matter.
719 *Geochimica et Cosmochimica Acta* 241:17-37.

720 Rubin A. E., Zolensky M. E., and Bodnar R. J. 2002. The halite - bearing Zag and Monahans (1998)
721 meteorite breccias: Shock metamorphism, thermal metamorphism and aqueous alteration on
722 the H - chondrite parent body. *Meteoritics & Planetary Science* 37:125-141.

723 Salisbury J. W., Walter L. S., Vergo N., and D'Aria D. M. 1991. *Infrared (2.1–25 micrometers) spectra*
724 *of minerals*. John Hopkins University Press, Baltimore.

725 Schimmelmann A., Qi H., Coplen T. B., Brand W. A., Fong J., Meier-Augenstein W., Kemp H. F.,
726 Toman B., Ackermann A., and Assonov S. 2016. Organic reference materials for hydrogen,
727 carbon, and nitrogen stable isotope-ratio measurements: caffeine, *n*-alkanes, fatty acid methyl
728 esters, glycines, L-valines, polyethylenes, and oils. *Analytical Chemistry* 88:4294-4302.

729 Schmitt-Kopplin P., Gabelica Z., Gougeon R. D., Fekete A., Kanawati B., Harir M., Gebefuegi I.,
730 Eckel G., and Hertkorn N. 2010. High molecular diversity of extraterrestrial organic matter in
731 Murchison meteorite revealed 40 years after its fall. *Proceedings of the National Academy of*
732 *Sciences of the United States of America* 107:2763-2768.

733 Scott E. R. D., Taylor G. J., and Keil K. 1993. Origin of ureilite meteorites and implications for
734 planetary accretion. *Geophysical Research Letters* 20:415-418.

735 Tayasu I., Hirasawa R., Ogawa N. O., Ohkouchi N., and Yamada K. 2011. New organic reference
736 materials for carbon-and nitrogen-stable isotope ratio measurements provided by Center for
737 Ecological Research, Kyoto University, and Institute of Biogeosciences, Japan Agency for
738 Marine-Earth Science and Technology. *Limnology* 12:261-266.

739 van Aken P. A. and Liebscher B. 2002. Quantification of ferrous/ferric ratios in minerals: new
740 evaluation schemes of Fe L23electron energy-loss near-edge spectra. *Physics and Chemistry*
741 *of Minerals* 29:188-200.

742 Vinogradoff V., Le Guillou C., Bernard S., Binet L., Cartigny P., Brearley A. J., and Remusat L. 2017.
743 Paris vs. Murchison: Impact of hydrothermal alteration on organic matter in CM chondrites.
744 *Geochimica et Cosmochimica Acta* 212:234-252.

745 Visser R., John T., Menneken M., Patzek M., and Bischoff A. 2018. Temperature constraints by Raman
746 spectroscopy of organic matter in volatile-rich clasts and carbonaceous chondrites. *Geochimica*
747 *et Cosmochimica Acta* 241:38-55.

748 Vollmer C., Kepaptsoglou D., Leitner J., Busemann H., Spring N. H., Ramasse Q. M., Hoppe P., and
749 Nittler L. R. 2014. Fluid-induced organic synthesis in the solar nebula recorded in
750 extraterrestrial dust from meteorites. *Proceedings of the National Academy of Sciences of the*
751 *United States of America* 111:15338-15343.

752 Warren P. H. and Kallemeyn G. W. 1992. Explosive volcanism and the graphite oxygen fugacity buffer
753 on the parent asteroid(s) of the ureilite meteorites. *Icarus* 100:110-126.

754 Zolensky M. E., Bodnar R. J., Yurimoto H., Itoh S., Fries M., Steele A., Chan Q. H.-S., Tsuchiyama
755 A., Kebukawa Y., and Ito M. 2017. The search for and analysis of direct samples of early Solar
756 System aqueous fluids. *Philosophical Transactions of the Royal Society A* 375:20150386.

757

758